

# Experimental Study on the Optimization of Multi-level Nano–Microsphere Deep Profile Control in the Process of Gas Injection in Fracture-Type Buried-Hill Reservoirs

Renyi Lin,\* Pingya Luo, Yang Sun, Yi Pan, and Lei Sun



Cite This: *ACS Omega* 2021, 6, 24185–24195



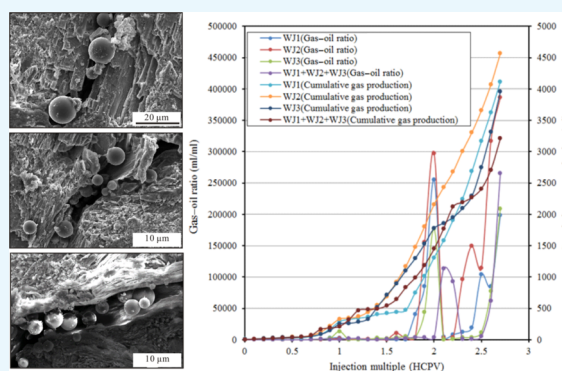
Read Online

ACCESS |

Metrics & More

Article Recommendations

**ABSTRACT:** Fracture-type buried-hill reservoirs refer to dual media which have a fast breakthrough speed and a low sweep efficiency in the process of gas injection displacement. In order to overcome this problem, in this paper, a new profile control and oil displacement technology of pre-plug deep plugging by injection of different levels of nano–microspheres and natural gas was proposed. The mercury intrusion experiments were used to compare the fractal characteristics of the pore structures of the matrix and artificial fractured cores in the buried-hill reservoir. The results show that the heterogeneous characteristics of pores and fractures are the main factors leading to excessive gas breakthrough. Three nano–microsphere systems (WJ1, WJ2, and WJ3) with good temperature resistance, salt resistance, swelling properties, and stability were prepared using the inverse emulsion method. Core plugging performance tests show that WJ3 has the best plugging effect among the three nano–microsphere systems, followed by WJ2 and WJ1. According to the scanning electron microscopy observations, it was found that the sealing mechanism of nano–microspheres includes direct sealing, bridging sealing, adhesive sealing, direct pass, deformed pass, and crushing pass. Finally, the displacement experiments with a composite fractured core showed that compared with pure natural gas injection, the breakthrough time of the combined displacement process of nano–microspheres and natural gas was greatly extended, and the final oil displacement efficiency was increased to greater than 80%.



## 1. INTRODUCTION

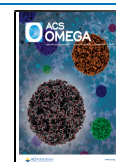
Fracture-type buried-hill reservoirs have dual media characteristics. The matrix reservoir is the main storage space, and the fracture network system is the main seepage channel for crude oil migration.<sup>1–4</sup> Gas injection oil displacement is a common development method for enhancing oil recovery for this type of reservoir.<sup>5–8</sup> Due to the high permeability features of the fracture networks, the displacement medium will quickly break through the high-permeability fracture channel, thus resulting in a low sweep efficiency.<sup>9–14</sup> Pure gas injection will always result in a large amount of remaining oil in the matrix, and the oil recovery rate will be greatly reduced.<sup>15–18</sup> Therefore, new injection and production technologies need to be adopted.

The key to the development of fractured reservoirs is to improve the oil sweep efficiency in the matrix pores.<sup>19–22</sup> Therefore, in order to realize the displacement of oil, it is necessary to properly plug the superior seepage channels such as fractures and large pores.<sup>23–26</sup> This requires the application of effective plugging profile control and oil displacement technology.<sup>27,28</sup> At present, the field application effect of the deep profile control and displacement technology of injecting polymer microspheres is generally good.<sup>2–5</sup> According to the

particle size of the microspheres, they have five passing modes in the reservoir, namely, direct passing, deformed passing, shear separation passing, bridging passing, and adhesive passing.<sup>2,3</sup> Therefore, the microspheres can be well adapted to the complex pore–fracture network structures of fracture-type buried-hill reservoirs.<sup>29–33</sup> After the microspheres enter the core sample, they can enter the deep part of the fracture network to achieve multi-dimensional step-by-step sealing and step-by-step profile control.<sup>3–5</sup> Lei and Zheng (2007)<sup>4</sup> found that the microspheres in the pores rely on the resistance of physical barriers to make water flow expand their swept volume. In addition, the elasticity of the microspheres allows the microspheres to pass through the front throats under the action of elastic deformation and restore their shapes at the back throats to generate resistance to the water flow again and

Received: July 14, 2021

Published: September 7, 2021



thus continuously migrate to the deep part of the oil layer. Liu and An (2010)<sup>5</sup> found that nano–micron polymer microspheres will expand and bond with each other during the process of deep profile control and displacement, and they will preferentially seal the high permeability formation. Fan and Cheng (2012)<sup>6</sup> systematically studied the turning characteristics of the streamlines before and after the plugging tests of polymer microspheres and adopted effective measures to adjust and develop the originally inactive low-permeability layers. Ultimately, the sweep coefficient of the injected water and the output of the oil wells were significantly increased.

Fracture-type reservoirs have become an important field for stable production in many oilfields.<sup>34–37</sup> However, they have difficulty in improving crude oil recovery. Both gas and microsphere injection can effectively improve crude oil recovery. In this paper, high-pressure mercury intrusion and fractal theory were used to analyze the pore structures of reservoir rocks. Moreover, the inverse emulsion method was used to prepare three nano–microsphere systems with different particle sizes, and the plugging performance of the microsphere system was evaluated through core flow experiments. Through this study, the microscopic plugging mechanism of the microsphere deep profile control and displacement has been clarified. Meanwhile, the effectiveness of microsphere injection for deep profile control displacement in fracture-type buried-hill reservoirs was verified.

## 2. MATERIALS AND METHODS

The rock and oil samples in this study were all collected from the metamorphic buried-hill reservoir in the Bongor Basin, with a buried depth of 1.300–1.600 m.

**2.1. Experimental Materials.** **2.1.1. Fluid Material.** Ground degassed crude oil, natural gas, and compound formation water (salinity 1.460 mg/L) were the fluid materials.

**2.1.2. Core Material.** The matrix cores were taken from the fracture-type buried-hill reservoir, and the size and petrophysical parameters of the matrix core used in the mercury intrusion experiments are shown in Table 1.

**Table 1. Core Parameters of the Mercury Intrusion Experiment**

serial number	core type	core length (cm)	core diameter (cm)	porosity (%)	permeability (mD)
1	matrix core	4.980	2.560	1.10	0.079
2	artificial fractured core	5.007	2.542	4.58	132.000

Meanwhile, the cores used in the fluid flow experiments are all artificial fracture cores, and the size and petrophysical parameters are shown in Table 2. In this paper, artificial fractures were made with reference to the permeability range of the real reservoir, and the porosity and permeability of the selected cores were within the real reservoir's porosity and permeability range.

**2.1.3. Nano–Microspheres.** In the laboratory, the inverse emulsion method was used to prepare three kinds of nano–microspheres (WJ1, WJ2, and WJ3). The raw materials used for nano–microsphere preparation include acrylamide, 2-acrylamide-2-methylpropanesulfonic acid, white oil, emulsifier, etc. Moreover, a laser particle size analyzer was used to measure the particle size distribution of the three nano–

**Table 2. Parameters of the Long Core (Artificial Fractured Core)**

serial number	core length (cm)	core diameter (cm)	porosity (%)	permeability (mD)
1	4.933	2.567	5.06	98.55
2	5.012	2.545	4.24	109.32
3	5.006	2.542	4.17	109.44
4	5.002	2.548	4.47	97.01
5	4.98	2.539	4.19	120.93
6	4.459	2.568	5.10	122.39
7	5.017	2.534	4.84	78.03
8	4.911	2.523	5.48	124.13
9	4.991	2.571	4.62	124.95
10	4.595	2.531	5.70	75.54
11	5.009	2.547	4.24	127.78
12	5.008	2.545	4.06	127.95
13	5.014	2.542	4.43	128.41
14	5.012	2.526	5.10	54.16
15	5.001	2.538	4.64	128.48
16	5.006	2.542	4.76	131.98

microsphere systems, and the median particle sizes of the nano–microspheres were 100 nm (WJ1), 300 nm (WJ2), and 800 nm (WJ3). These three kinds of nano–microspheres were all prepared into a solution with a salinity of 1.460 mg/L, and they were aged for 90 days at a reservoir temperature of 96.8 °C. After aging, the water-swelling particle size of the microspheres increased, and they maintained a good spherical shape without deformation or water-absorbing ruptures, indicating that the nano–microspheres have good temperature and salt resistance properties. An optical microscope was used to observe the expanded morphology of nano–microspheres, and a laser particle size analyzer was used to determine the size distribution of the expanded microspheres. It can be seen from Figure 1 that after the nano–microspheres were fully expanded, the appearance of the polymer microspheres was round, and the particle size of the microspheres was several to several tens of times the original size. The existence of the microsphere particles is generally a free state, so the microspheres can enter the core step by step, and then, they will seal the pores matching the particle size of the microspheres. However, the existence of multiple particles in a polymerized state indicates that the microspheres have secondary cross-linking during the expansion process. For large pores, microspheres can be blocked by continuous aggregation and enlargement through secondary cross-linking. The combination of the above two plugging forms can achieve the purpose of deep profile control and oil displacement. In this paper, the plugging of microspheres and natural gas injection were combined to form a new injection–production scheme to improve oil recovery.

**2.2. High-Pressure Mercury Intrusion Experiment.** The high-pressure mercury porosimeter used in this research is an AutoPore IV 9520, and its pressure range is between 200 and 400 MPa. Mercury can enter the pores by applying pressure, so the higher the pressure, the smaller the pore diameters that mercury can enter. During the experiment, different external pressures and mercury volumes were recorded, and the Washburn equation was used to calculate the pore size distribution and pore volume.<sup>7,8</sup>

**2.3. Plugging Performance Experiment of Multi-level Nano–Microspheres.** Three artificial cores were selected to

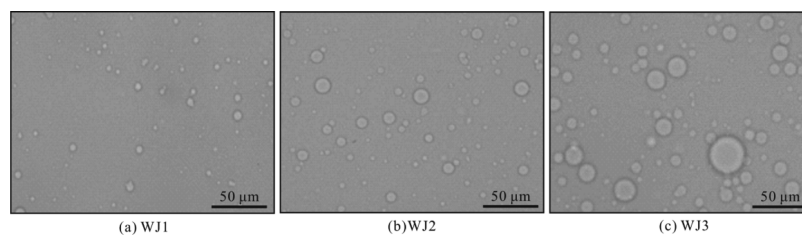


**Figure 1.** Swelling morphology of microspheres of different samples. Notes: (a) WJ1, 100 nm median particle size; (b) WJ2, 300 nm median particle size; and (c) WJ3, 800 nm median particle size.

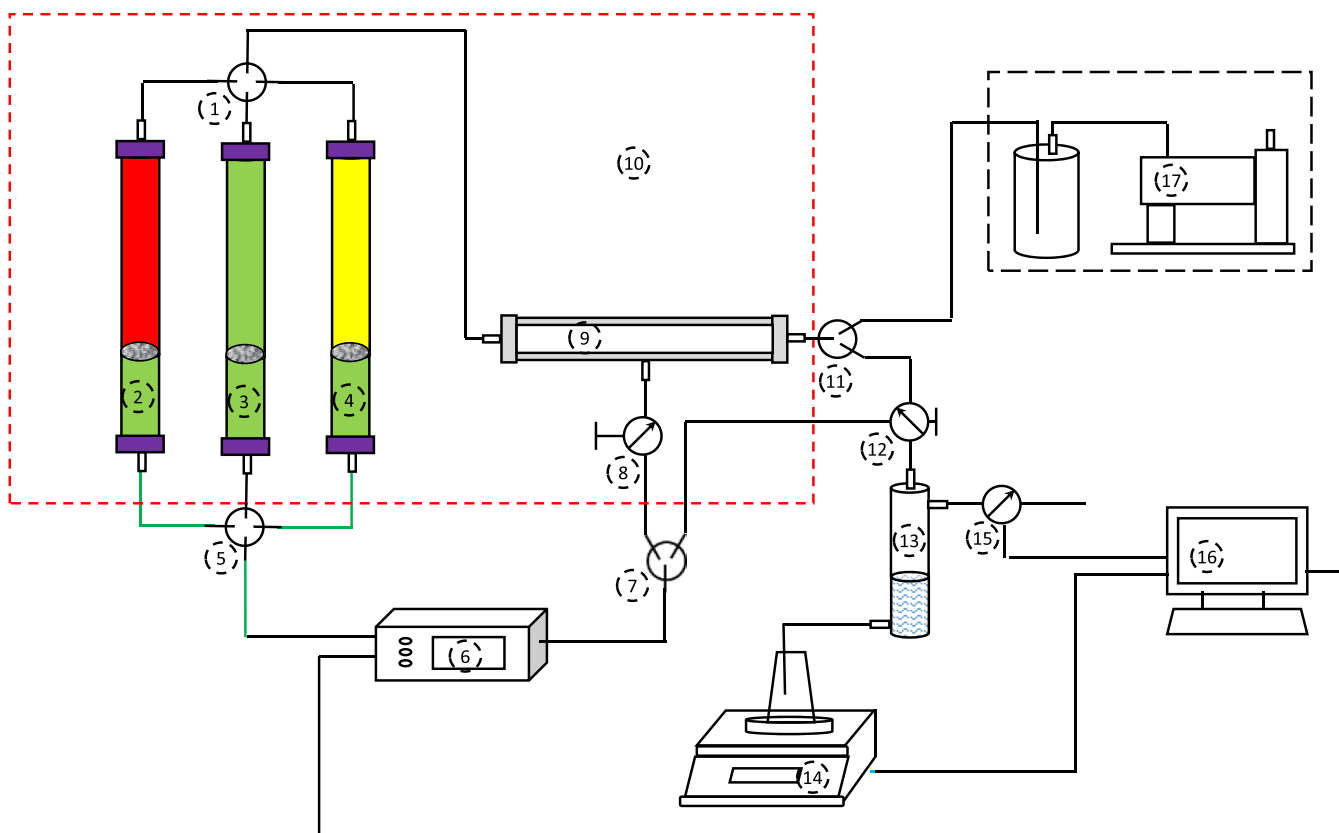


**Figure 2.** Schematic diagram of the multi-level sub-nano-microsphere deep profile control and oil displacement experimental device. Notes: 1—four-way shut-off valve; 2—oil piston cylinder; 3—water piston cylinder; 4—N<sub>2</sub> piston cylinder; 5—four-way shut-off valve; 6—advection pump; 7—three-way shut-off valve; 8—ring pressure valve; 9—long core holder; 10—constant temperature system; 11—three-way shut-off valve; 12—gas flow meter; 13—gas-liquid separation device; 14—electronic balance instrument; 15—gas flow meter; 16—computer; 17—vacuum pump.

carry out microsphere plugging performance experiments at a reservoir temperature of 96.8 °C. First, the permeability  $k_1$  of the core sample saturated with formation water was measured, and the displacement pressure  $p_1$  when the displacement kept stable was recorded; then, the polymer microspheres were injected into the core, and the recorded injection pressure is  $p_2$ . After the microspheres were gelled, the simulated formation water was injected to displace 4–6 PV, and the stable displacement pressure  $p_3$  was recorded. Finally, the core permeability  $k_2$ , residual resistance coefficient, and plugging rate were determined<sup>9,10</sup>

$$F_{RR} = \frac{\Delta P_3}{\Delta P_1} \quad (1)$$

$$\eta = \frac{k_1 - k_2}{k_1} \times 100\% \quad (2)$$

Among them,  $F_{RR}$  is the residual resistance coefficient,  $\Delta P_1$  is the stable injection pressure difference of water displacement,  $\Delta P_3$  is the subsequent stable injection pressure difference of water displacement, and  $\eta$  is the plugging rate.

In the synthesis process of microspheres, the Box–Behnken method was used to analyze the content of components in various formulations, and then, the optimal product was obtained. In the fluid flow experiments, a field emission environmental scanning electron microscope produced by FEI was used to observe the sealing performance of the rock samples. This equipment can perform nanolevel three-dimensional observations without damaging the samples.

## 2.4. Deep Profile Control and Oil Displacement Experiments Using Multi-level Nano-Microspheres.

**2.4.1. Core Number.** The arrangement of the cores in the long core holder referred to formula 3, and the sorted cores were placed in order from the outlet to the inlet.<sup>11,12</sup> At the same time, filter paper was added at the junction of each core

**Table 3. Test Results of Mercury Intrusion Characteristic Parameters of Test Cores**

core type	mean coefficient	sorting coefficient	skew factor	variable coefficient	average pore throat radius ( $\mu\text{m}$ )	maximum mercury saturation (%)	mercury removal efficiency (%)
matrix core	13.2164	1.7767	0.6739	0.1344	0.1222	74.8308	32.6440
artificial fractured core	16.3294	2.6397	-2.4551	0.1617	0.2178	90.5973	24.8938

end face to eliminate the interface effect.<sup>13</sup> The basic information of the cores is shown in Table 2, and the experimental process is shown in Figure 2

$$\frac{L}{\bar{K}} = \frac{L_1}{K_1} + \frac{L_2}{K_2} + \dots + \frac{L_i}{K_i} + \dots + \frac{L_n}{K_n} = \sum_{i=1}^n \frac{L_i}{K_i} \quad (3)$$

In the formula,  $L$  is the total length of the core, cm;  $\bar{K}$  is the harmonized average permeability of the core, mD;  $L_i$  is the length of the  $i$ -th core, cm; and  $K_i$  is the permeability of the  $i$ -th core, mD.

**2.4.2. Formation Crude Oil Preparation.** The formation oil was prepared according to the gas–oil ratio (GOR) of the crude oil obtained on site, and the natural gas used in the prepared crude oil was consistent with the composition of the on-site separated gas according to chromatographic analysis. The specific method is as follows: first, 600 mL of surface oil was prepared, and then, the required separator gas volume was calculated according to the original production GOR. Finally, the crude oil samples were prepared in the sampler according to the original formation pressure.

**2.4.3. Establishment of Irreducible Water Saturation.** The method of quantitatively establishing irreducible water saturation in this paper is as follows: (1) first, the pore volume of the core sample was calculated according to the porosity and permeability parameters; (2) the amount of irreducible water to be injected was calculated based on the irreducible water saturation provided by the oilfield. Finally, the calculated volume of water was injected into the core. In this study, the irreducible water saturation ( $S_{wi} = 0.32$ ) was established quantitatively when the formation temperature was 96.8 °C. By recording the volume of injected water, it was obtained that the actual pore volume was 8.33 mL and the hydrocarbon pore volume was 5.83 mL.

**2.4.4. Establishment of Original Oil Saturation.** The dead oil was saturated at the experimental temperature of 96.8 °C, and the pressure was increased to the original formation pressure of 12.3 MPa. At the same time, the oil-saturated core was placed in a core holder for more than 3 days under the experimental temperature and pressure. The configured live oil was used to displace the core, and the oil and gas volumes were recorded at the outlet end at regular intervals. Then, the original GOR was calculated.

**2.4.5. Experimental Process.** Natural gas injection and oil displacement: first, natural gas was injected at a rate of 2 MPa/h until the pressure drops to 7.7 MPa. Under 7.7 MPa, natural gas was injected into the core at a rate of 0.06 mL/min, and the displacement was stopped after it no longer produced oil. When the outlet no longer produced oil, the outlet valve was closed to stop the oil displacement. Then, the natural gas was used to maintain a constant pressure of 7.7 MPa for 24 h. After 24 h, the oil displacement via natural gas injection will continue. That is, natural gas was injected into the core at a rate of 0.06 mL/min until the end. Similarly, when the outlet no longer produces oil, the outlet valve will be closed, and the natural gas was used to increase the pressure to 12.3 MPa for

24 h before continuing to conduct oil displacement. At this time, natural gas was injected into the core at a rate of 0.06 mL/min until the end.

Combined displacement of nano–microsphere (WJ1, WJ2, or WJ3) and natural gas injection: first, nano–microspheres and natural gas were injected at a rate of 2 MPa/h until the pressure dropped to 7.7 MPa. Below 7.7 MPa, WJ1 (or WJ2 or WJ3) microsphere solution with a concentration of 0.2 HCPV was injected into the core at a rate of 0.06 mL/min. When the microsphere solution can be seen in the outlet section, the displacement will stop and the well will be soaked until the microspheres are fully expanded. Below 7.7 MPa, natural gas will be injected into the core at a rate of 0.06 mL/min until it no longer produces oil. Similarly, when the outlet no longer produces oil, the outlet valve will be closed, and the natural gas is used to increase the pressure to 12.3 MPa for 24 h before continuing to conduct oil displacement. Then, the natural gas will be injected into the core at a rate of 0.06 mL/min until the end.

Combined oil displacement of microsphere combination (WJ1 + WJ2 + WJ3) and natural gas injection: first, combined microspheres and natural gas were injected at a rate of 2 MPa/h until the pressure dropped to 7.7 MPa. Under 7.7 MPa, the WJ1, WJ2, and WJ3 microsphere solution slugs of a concentration of 0.1 HCPV were injected into the core three times at a rate of 0.06 mL/min. When 0.3 HCPV natural gas was injected each time and the slug was replaced deeper in the core, the displacement was stopped. Finally, the microspheres were fully expanded. The subsequent displacement process is the same as the plugging process of injecting a single type of microsphere.

In this research, a pure natural gas displacement and a combined displacement of nano–microsphere and natural gas injection were conducted. After each experiment, the core was cleaned with petroleum ether and alcohol, and then, the core was blown dry with nitrogen and evacuated with a vacuum pump.

### 3. RESULTS

**3.1. High-Pressure Mercury Intrusion Results.** Table 3 shows the results of mercury intrusion parameters obtained through high-pressure mercury intrusion experiments, which include mean coefficient, sorting coefficient, skew factor, variation coefficient, pore throat radius, maximum mercury saturation, and mercury removal efficiency. It can be seen that the maximum mercury saturation of the matrix core and the artificial fractured core are 74.8308 and 90.5973%, respectively, and the mercury removal efficiencies of them are 32.6440 and 24.8938%, respectively.

**3.2. Plugging Performance of Multi-level Nano–Microspheres.** Figure 3 shows the plugging performance test results of different levels of nano–microspheres, and Table 4 shows the permeability changes of the experimental cores before and after the microspheres were injected. It can be calculated that the residual resistance coefficient of the sample

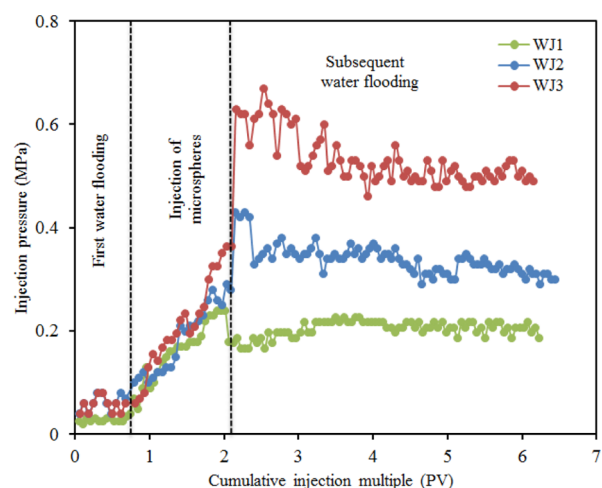


**Figure 3.** Relationship between injection multiple PV and injection pressure of the samples.

with WJ1 microsphere injection is 5.35, and its plugging rate is 49.46%. After WJ2 microspheres are injected, the residual resistance coefficient of the sample is 6.22, and the plugging rate is 69.8%. After WJ3 microspheres are injected, the residual resistance coefficient of the sample is 9.09, and the blocking rate is 88.6%.

It can be seen from Figure 3 that when WJ1–WJ3 nanospheres were injected into the core, the injection pressure in the core changed greatly. This is because when the microspheres enter the core, they will physically block the pore throats of the core. This process is like the “Jamin effect” of bubbles at the throats, which will produce an additional resistance. When the pressure increases to a certain value, the microspheres deform and pass through the throats and the pressure drops. Similarly, the microspheres will move to the back thin throats and will be blocked again, and then, the “wave pressure change” shown in Figure 3 will appear. WJ3 has the largest particle size, and the experimental results show that the plugging effect of WJ3 is the best. Therefore, compared with WJ1 and WJ2, the fluctuating pressure change when WJ3 is injected is the most obvious.

In addition, when the microspheres were injected into the core, they experienced a sharp linear increase when the injection pressure was before 0.5 HCPV. This indicates that the microspheres had already begun to expand during the injection process, and the microspheres were trapped in the core pores, resulting in a sharp increase in injection pressure (Figure 3).

### 3.3. Multi-level Nano–Microsphere Deep Profile Control and Oil Displacement.

**3.3.1. Pure Natural Gas Injection.** The cores in Table 2 were used to conduct the oil displacement experiment, and the combined core had a harmonic average permeability of 103.58 mD. In the process of pure natural gas injection, the oil displaced by the soaking well was 5.75%, and the final oil displacement efficiency was

66.35%. Figures 4 and 5 show the relationship between injection multiples and oil displacement efficiency, GOR, and

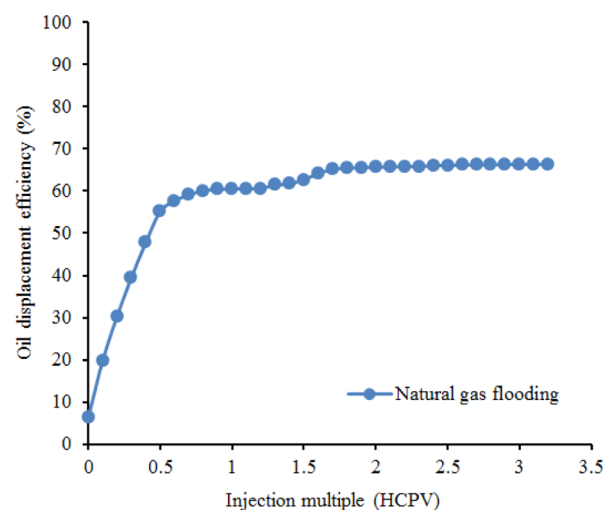


**Figure 4.** Relationship between injection multiples and oil displacement efficiency.

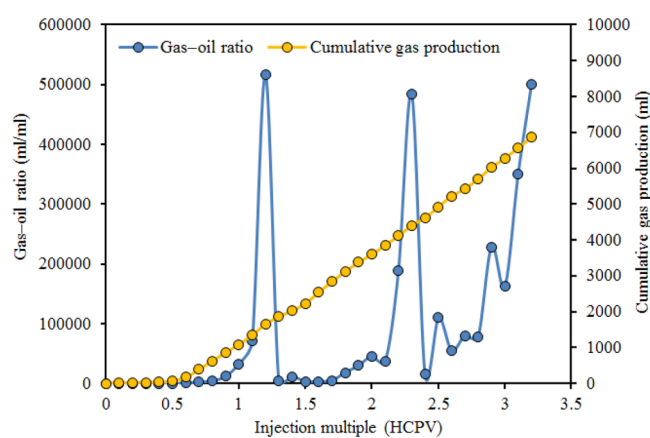


**Figure 5.** Relationship between injection multiples, GOR, and cumulative gas production.

cumulative gas production. It can be seen that the breakthrough was achieved only when a 0.6 HCPV volume was injected during the natural gas injection process.

From Figure 4, it can be seen that during the microsphere injection process, the injection pressure experienced a sharp linear increase before 0.5 HCPV. This indicates that the microspheres had already begun to expand during the injection process. Then, the pores were blocked, which in turn leads to a sharp increase of the injection pressure.

**3.3.2. Multi-level Deep Profile Control and Displacement with Nano–Microspheres.** Figure 6 shows the relationship between injection multiples and oil displacement efficiency. During the deep profile control and displacement process of

**Table 4.** Changes of Parameters before and after Core Plugging

core number	gas permeability (mD)	liquid permeability (mD)	types of microspheres	liquid permeability (after the experiment, mD)	residual resistance factor	plugging rate (%)
1	87.15	12.15	WJ1	6.14	5.35	49.46
2	83.20	10.20	WJ2	3.08	6.22	69.80
3	82.44	10.44	WJ3	1.19	9.09	88.6

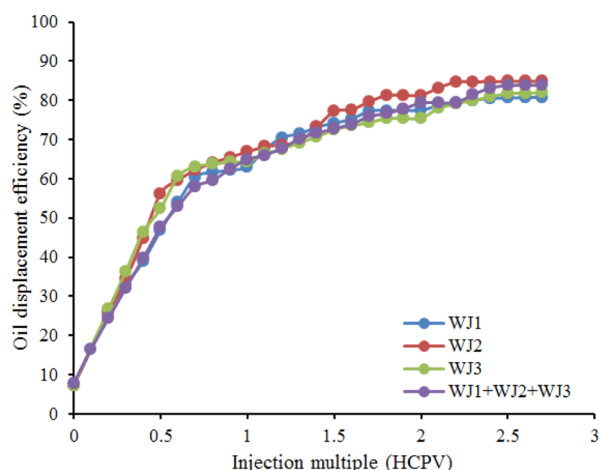


**Figure 6.** Relationship between injection multiples and oil displacement efficiency of different types of samples.

different levels of nano-microspheres, the oil displaced by the WJ1 microsphere was 17.75%, and the final oil displacement efficiency was 80.77%; the oil displaced by the soaked well with WJ2 microspheres was 17.51%, and the final oil displacement efficiency was 81.94%; the oil displaced by the soaked well injected with WJ3 microspheres was 18.02%, and the final oil displacement efficiency was 84.91%; and the oil displaced by the soaked well with three kinds of microspheres was 16.14%, and the final oil displacement efficiency was 83.93%. [Figure 7](#)

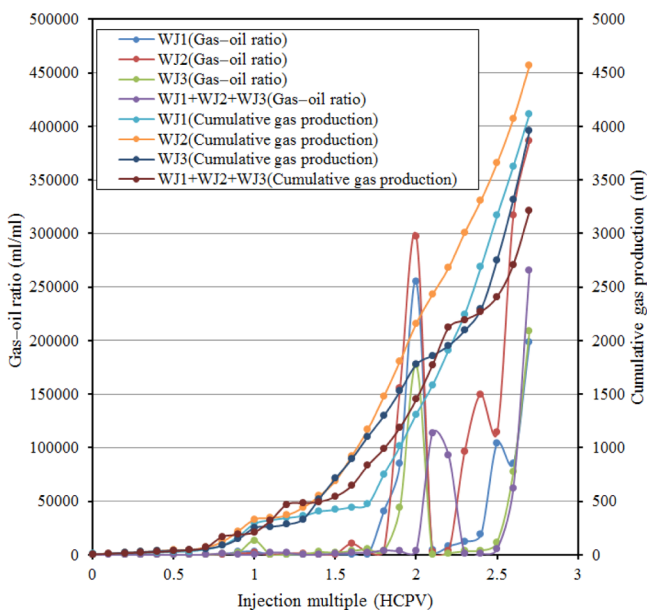


**Figure 7.** Relationship between injection multiples, GOR, and gas production of different types of samples.

shows the relationship between injection multiples, GOR, and cumulative gas production. It can be seen that the natural gas injection process achieved a breakthrough when a 0.7 HCPV volume was injected.

## 4. DISCUSSION

**4.1. Analysis of Pore Structures and Pore Fractal Features.** The matrix core (no. 1 sample) and the artificial fractured core (no. 2 sample) in [Table 1](#) were used to carry out

high-pressure mercury intrusion experiments. It can be seen from [Table 3](#) that the mean coefficients of the matrix core and the artificial fractured core are very large, which indicates that micropores are mainly developed in the matrix and artificial fractured cores. The sorting and skew coefficients of the cores are relatively large, and the variation coefficients are relatively small. The larger the sorting coefficient, the more uneven the pore distribution of the cores. According to the test results, the absolute value of the skew coefficient of the artificial fractured core is larger than that of the matrix core, indicating that the internal pore distribution of the artificial core is more asymmetric. In addition, the variation coefficient of the samples is small, indicating that the pore-throat coupling and connectivity in the cores are poor.<sup>38–42</sup> It can be seen from [Figure 8](#) that the pore throats of the matrix core are mainly

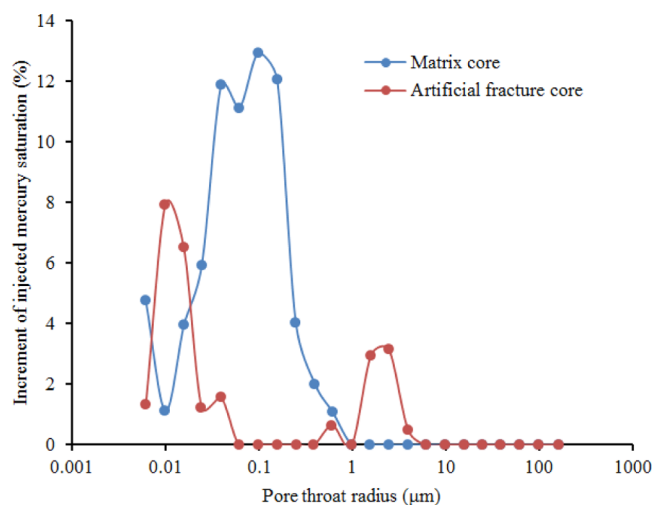


**Figure 8.** Distribution of pore throat radius of different types of samples.

distributed between 0.1 and 1  $\mu\text{m}$ . However, the pore throat distribution of the artificial fractured core is mainly concentrated in two intervals; one part is a small pore throat between 0.01 and 0.1  $\mu\text{m}$ , and the other part is a large pore interval between 1 and 10  $\mu\text{m}$ . On the whole, the heterogeneity of the artificial core is stronger than that of the matrix core.<sup>43,44</sup>

According to [Figure 9](#), the mercury removal curve of the artificial fractured core exhibited a sudden or straight drop. This indicates that micropores are mainly developed in the artificial core, and the proportion of fine-necked pores is very high. Since the connectivity between the pores is poor, the mercury removal efficiency is low ([Figure 9](#)).<sup>45–51</sup> Poor connectivity within the core is the result of a combination of various reservoir factors, such as pore size, pore-to-throat ratio, microfractures, and heterogeneity.<sup>49–52</sup> The combined effect of these factors leads to a low mercury removal efficiency, and a large amount of mercury remains in the pores. Therefore, in the process of oilfield development, a large amount of remaining oil cannot be produced.<sup>43,44</sup>

The results of high-pressure mercury intrusion experiments and the fractal principle were used to analyze the fractal characteristics of pore structures. According to the fractal principle, there is a power law between the number of objects and the measurement scale. Then, the relationship between the number  $N$  with the same pore radius and the pore radius  $r$  is<sup>14</sup>

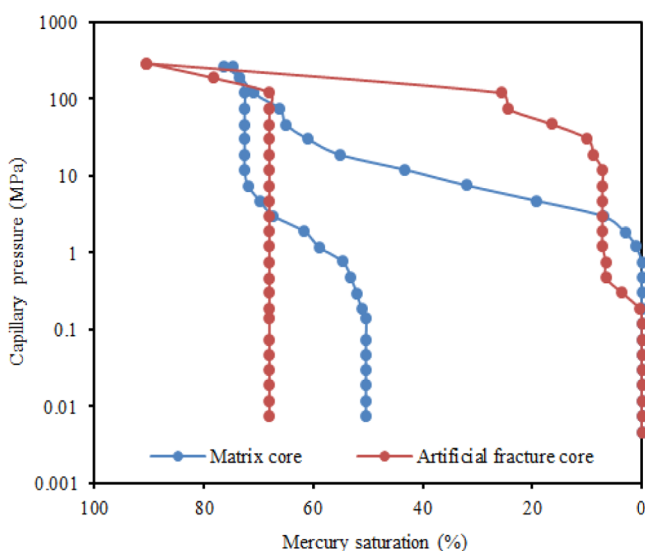


**Figure 9.** Comparison of mercury injection curves of the matrix core and artificial fractured core.

$$N(r) = ar^{-D} \quad (4)$$

In the formula,  $a$  is the constant of proportionality and  $D$  is the fractal dimension.

According to the Brooks–Corey model, it is assumed that the rock pore space is composed of a series of capillary bundles.<sup>15</sup> Therefore, the cumulative volume percentage of the pore radius smaller than  $r$  can be expressed as<sup>16–18</sup>

$$V_c = \left( \frac{r}{r_{\max}} \right)^{3-D} \quad (5)$$

In the formula,  $r$  is the pore radius.

For a cylindrical pore with a radius of  $r$ , the mercury inlet pressure ( $P_c$ ) is related to the surface tension ( $\sigma$ ) and contact angle ( $\theta$ ) between the injected fluid and the replacement fluid

$$P_c = \frac{2\sigma \cos \theta}{r} \quad (6)$$

$P_c$  and  $r$  are inversely proportional; then,  $P_{\min} = 2\sigma \cos \theta / r_{\max}$  and we can get

$$V_c = \left( \frac{r}{r_{\max}} \right)^{3-D} = \left( \frac{P_c}{P_{\min}} \right)^{D-3} \quad (7)$$

Taking the logarithm of both sides, we can get

$$\log V_c = (D - 3)\log P_c - (D - 3)\log P_{\min} \quad (8)$$

In the above formula,  $\log V_c$  has a linear relationship with  $\log P_c$ . The relationship between  $\log V_c$  and  $\log P_c$  of the matrix core and artificial fractured core is shown in Figure 10. According to the slope of the curve, the pore fractal dimension can be calculated (Table 5).

The fractal dimensions of the matrix and artificial fractured cores are between 2 and 3. Generally, the closer the fractal dimension of the core is to 2, the stronger the pore homogeneity, and the closer it is to 3, the more complex the pore structures. In Table 5, the fractal dimension of the matrix core is significantly smaller than the fractal dimension of the artificial fractured core, indicating that the pore structures of the artificial fractured core are much more complicated than

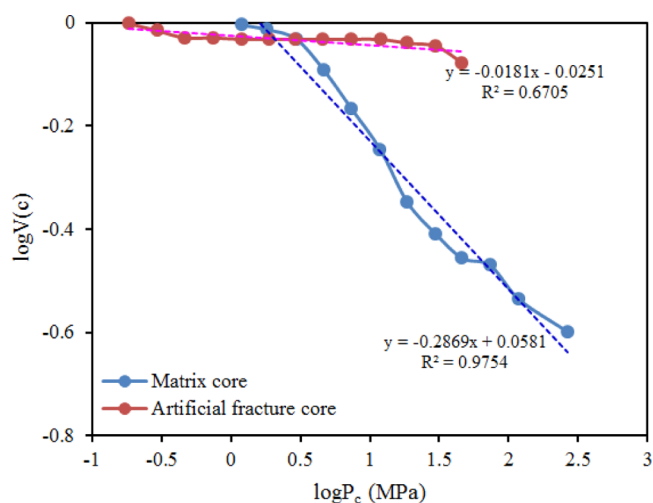


**Figure 10.** Relationship between  $\log V_c$  and  $\log P_c$  of the matrix core and artificial fractured core.

**Table 5.** Calculation Results of Fractal Dimensions of the Samples

core type	fitting function	correlation coefficient ( $R^2$ )	$D$
matrix core	$\log V_c = -0.2869 \log P_c + 0.0581$	0.975 4	2.713 1
artificial fractured core	$\log V_c = -0.0181 \log P_c - 0.0251$	0.670 5	2.981 9

the matrix core. Although artificial fractures can increase the fluid circulation channels in the core, they can also increase the complexity of the pore structures, so the “water channeling” phenomenon during the crude oil displacement process will be more serious.

**4.2. Analysis of Plugging Performance of Multi-level Nano–Microspheres.** The plugging performance of nano–microsphere particles can be significantly affected by the high temperature and the high salt environment. They can gradually expand and partially stay in the pores, causing pore plugging. Furthermore, the permeability of the cores will decrease to varying degrees, and the fluid flow resistance will increase. For a specific reservoir, the plugging effect of the microsphere solution is related to the ability of the microsphere solution to reduce the rock permeability. In the process of microsphere injection, the permeability decrease coefficient (or residual resistance coefficient) is a quantitative indicator of the permeability decrease of the porous medium after the microsphere solution passes through the porous medium.

The calculated resistance coefficient and plugging rate are shown in Table 4. It can be seen that the injection of nanopolymer microspheres will block the pore throats and reduce the rock permeability. The larger the particle size of the nano–microspheres, the larger the residual resistance coefficient and the better the plugging effect. The experimental results show that the plugging effect of WJ3 microspheres is the best, which can reach 88.6%, followed by the WJ2 microspheres and the WJ1 microspheres.

**4.3. Blocking Mechanism of Nano–Microspheres.** The nano–microsphere system can enter the pores with the solution in the form of suspended particles. With the flow of the fluid, the nano–microspheres will first enter the pores connected by microfractures with high permeability, and then,

they will migrate between the pores. During the migration process, the microsphere particles will be affected by surface adsorption, mechanical trapping, hydrodynamic trapping, and the interaction between elastic microsphere particles. In addition, the microsphere system will also cause retention on the surface of the pores and in the throats. In these experiments, a scanning electron microscope was used to directly observe the plugging states of the microspheres. The results are shown in Figure 11. According to the observation

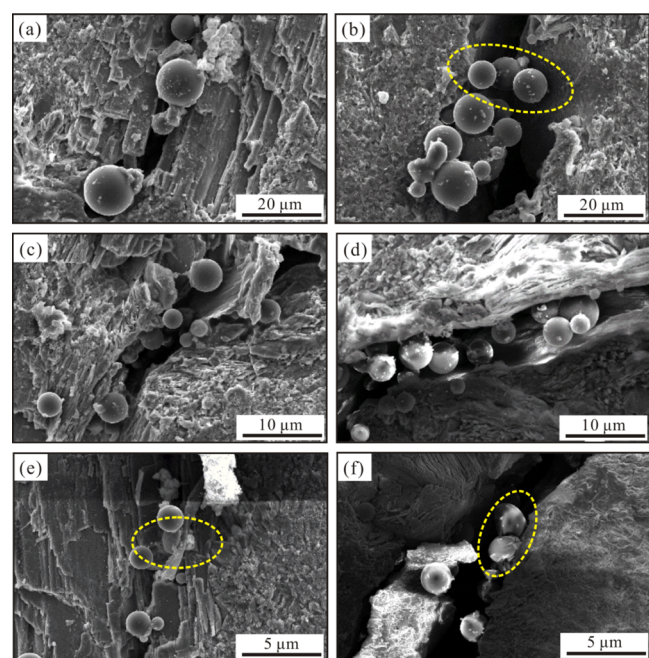


**Figure 11.** Blocking mechanism of nano-microspheres. Notes: (a) sample WJ3, blocking of a single microsphere; (b) sample WJ3, bridging blocking of multiple microspheres; (c) sample WJ2, adhesion; (d) sample WJ2, direct pass; (e) sample WJ1, deformation pass; (f) sample WJ1, crushing pass.

results, the blocking mechanism of the microsphere system includes direct sealing, bridging sealing, adhesive sealing, direct pass, deformed pass, and crushing pass.

**4.3.1. Direct Sealing of a Single Microsphere.** When the pore throat size is smaller than the particle size of a single microsphere particle, the microsphere particles will be trapped by the pore throat, and then the microsphere particles will stay in the pore throat entrance and block the throats (Figure 11a). The pore throat size, microsphere size, microsphere concentration, and fluid flow rate all affect the plugging performance of microspheres. When the pore throat size is a constant, the larger the particle size, the smaller the concentration of microspheres, and the greater the fluid flow rate, the easier the blocking of a single microsphere system will occur.

**4.3.2. Bridging Sealing of Multiple Microspheres.** When the pore throat size is larger than the particle size of the microspheres, multiple microsphere particles will aggregate together and block the pore throats through secondary cross-linking (Figure 11b). The higher the concentration of microsphere particles and the higher the cross-linking strength between microsphere particles, the greater the strength of bridging sealing.

**4.3.3. Adhesive Sealing.** The phenomenon that the microsphere particles adhere to the surface of the matrix or

cracks is actually because the microsphere particles are in a state of mechanical equilibrium. Since the resultant force of the microspheres is directed to the rock surface, the microspheres will adhere to the substrate or crack surface (Figure 11c). When the fluid velocity changes, this force balance may be broken, and the adhesion state of the microspheres will change.

**4.3.4. Direct Pass.** Direct pass of microspheres means that the particles of microspheres enter the pores of rock samples with the solution. When the particle size of the microspheres is smaller than the pore throat size, the microsphere particles will directly enter the cores through the pore throats (Figure 11d).

**4.3.5. Deformed Pass and Crushing Pass.** The microsphere particles in the pores and throats will be affected by the driving force of the fluids and the reaction force of the throat wall. Due to the elastic nature of the microsphere particles, when the driving force of the microspheres is greater than the reaction force of the throat wall, the microsphere particles will be elastically deformed and squeeze into the pore throats. The microsphere in the yellow circle shown in Figure 11e is deformed, and when the microsphere particle passes through the pore throat, it will return to its original spherical shape. Generally, the greater the driving force of the microspheres, the easier it is for them to pass through the pore throats.

If the driving force of the microsphere particles is too large and the pore throat size is too small, the microspheres will be broken due to excessive elastic deformation (Figure 11f). However, after the broken microsphere particles pass through the pore throats, they will re-form into smaller-particle-size microsphere particles.

**4.4. Analysis of the Effect of Multi-level Nano-Microspheres for Deep Profile Control and Oil Displacement.** The effect of natural gas injection in fracture-type buried-hill reservoirs is usually better. On the one hand, the gas is lighter and it can move to the upper part of the reservoir acting as a “gravity drainage”. On the other hand, natural gas is easily soluble in oil, so mass transfer will continue to occur at the oil-gas interface, thereby delaying the breakthrough time and improving oil displacement efficiency. Regarding the process of soaking wells, the oil production of soaking wells during the experiment of natural gas injection increased by 5.75%. This is due to the strong diffusion capacity of gas molecules, which can enter the tiny pores for mass exchange and drive out more crude oil.

For pure natural gas injection, the natural gas injection process achieved a breakthrough when 0.6 HCPV gas was injected. After the breakthrough, the gas production has gradually increased, and the GOR has risen rapidly. After the breakthrough of the injected gas, the subsequently injected gas will flow along the fractures and pore zones with high permeability, and the matrix with low permeability will hardly be affected again, which will result in the existence of a large amount of remaining oil. In order to further improve the recovery rate, we adopted the combined displacement technology of nano-microsphere and natural gas injection to increase the degree of crude oil recovery.

Compared with pure natural gas injection, the final oil displacement efficiency of the composite displacement of nanometer microspheres + natural gas injection is significantly improved. The oil displacement efficiency of the combined displacement has reached more than 80%; especially, the increase of the crude oil displaced after the soaking of the well is the largest. This is because the injection of microspheres will preferentially seal the fractures with high permeability in the

core, which in turn causes the subsequent injection of natural gas to divert to the matrix with low permeability. The composite displacement expands the range of diffusion, thereby improving the spread efficiency. In the process of soaking wells, due to the long contact time between natural gas and crude oil, the mass transfer effect of oil and gas is fully exerted so that the oil displacement efficiency can be improved.

Comparing the profile control and displacement results of injecting different types of nano-microsphere solutions, it was found that the overall trend was consistent with the results obtained from the microsphere performance tests. The best effect is the injection of WJ3 microsphere solution, followed by the injection of three types of microspheres and then by the WJ2 microsphere solution, and the worse is the WJ1 microsphere solution. The difference in application effect shows that the microspheres will be affected by the pore throat size and the particle size of the microspheres when they migrate in the pores. The Kozeny formula [formula 9] was used to estimate the average pore diameter of the original rock

$$r = \sqrt{\frac{8k}{\phi}} \quad (9)$$

where  $k$  is the permeability of the rock ( $\mu\text{m}^2$ ),  $\phi$  is the porosity of the rock, and  $r$  is the average pore throat radius of the rock ( $\mu\text{m}$ ).

Combined with Table 2, it can be calculated that the pore radius of the experimental cores is mainly distributed between 2.9 and 5.1  $\mu\text{m}$ . Only when the size of the microspheres is equal to or less than 2–3 times the pore diameter of the reservoir, the microspheres can effectively block the pores of the reservoir.<sup>18,19</sup> Only the WJ3 microspheres with a particle size of 800 nm are the most suitable for these conditions; therefore, the plugging effect is the best. The oil displacement efficiency of WJ3 microsphere injection is slightly higher than that of the microsphere injection combination, indicating that WJ3 nanospheres are more compatible with the core pore structures in this experiment.

The combined displacement of nano-microsphere and natural gas injection greatly prolongs the breakthrough time of the displacement process. The breakthrough process started from 0.7 HCPV, and the breakthrough was not fully realized until the injection multiple reached 2.2 HCPV. Combining Figures 6 and 7, it can be seen that during the gas breakthrough, the GOR in the early stage slowly increased, and the gas production gradually increased. When the breakthrough was about to complete, the GOR and gas production growth rate changed significantly. It greatly reduces the hazards caused by the rapid breakthrough of the injected gas, expands the scope of spread, and improves the final oil displacement efficiency. Finally, the effectiveness of deep profile control displacement with microsphere injection in fracture-type buried-hill reservoirs was verified.

## 5. CONCLUSIONS

- (1) In this paper, a new technology of pre-slug deep plugging by injection of different levels of nano-microspheres + natural gas injection combined with profile control and oil displacement is proposed.
- (2) The mercury intrusion experiments were used to compare the fractal characteristics of the pore structures of the matrix and artificial fractured cores in fracture-type buried-hill reservoirs. The results show that the

heterogeneous characteristics of pores and fractures are the main factors leading to excessive gas breakthrough during the development of fracture-type buried-hill reservoirs.

- (3) During the migration process, the microsphere particles will be affected by surface adsorption, mechanical trapping, hydrodynamic trapping, and the interaction between elastic microsphere particles. Furthermore, the microsphere system will cause retention on the pore surface and inside the pore throats. The plugging mechanism of microspheres in cores includes direct sealing, bridging sealing, adhesive sealing, direct pass, deformed pass, and crushing pass.
- (4) Through the core plugging performance tests, the plugging effect of the three nano-microspheres WJ1, WJ2, and WJ3 was verified. The selected microspheres WJ1, WJ2, and WJ3 can all achieve effective pore plugging, and the larger the particle size of the microspheres, the greater the residual resistance coefficient and the higher the plugging rate. WJ3 microspheres with a particle size of 800 nm have the best blocking effect, which can reach 88.6%.
- (5) For the pre-slug deep plugging by the injection of different levels of nano-microspheres + natural gas injection composite profile control and displacement, the pre-microspheres can effectively seal the large pores and fractures and high-permeability channels in the core, thereby effectively inhibiting the rapid breakthrough of the injected gas. In addition, it can induce the injected gas to change the flow direction, thereby greatly improving the oil displacement efficiency. Among them, the nano-microsphere WJ3 has the best matching with the pores of the artificial fractured core, and the oil displacement efficiency after plugging was the highest.
- (6) The multi-stage sub-nanosphere deep profile control and oil displacement technology proposed in this paper greatly prolongs the breakthrough time of the displacement process and reduces the damage caused by the rapid breakthrough of the injected gas. In addition, it also effectively expands the spread range and improves the final oil displacement efficiency.

## ■ AUTHOR INFORMATION

### Corresponding Author

**Renyi Lin** – The State Key Laboratory of Oil and Gas Reservoir Geology and Exploitation, Southwest Petroleum University, Chengdu, Sichuan 610500, China; [orcid.org/0000-0002-9808-7575](https://orcid.org/0000-0002-9808-7575); Email: [linrenyi122@163.com](mailto:linrenyi122@163.com)

### Authors

**Pingya Luo** – The State Key Laboratory of Oil and Gas Reservoir Geology and Exploitation, Southwest Petroleum University, Chengdu, Sichuan 610500, China

**Yang Sun** – The State Key Laboratory of Oil and Gas Reservoir Geology and Exploitation, Southwest Petroleum University, Chengdu, Sichuan 610500, China

**Yi Pan** – The State Key Laboratory of Oil and Gas Reservoir Geology and Exploitation, Southwest Petroleum University, Chengdu, Sichuan 610500, China

**Lei Sun** – The State Key Laboratory of Oil and Gas Reservoir Geology and Exploitation, Southwest Petroleum University, Chengdu, Sichuan 610500, China

Complete contact information is available at:  
<https://pubs.acs.org/10.1021/acsomega.1c03751>

## Notes

The authors declare no competing financial interest.

## ACKNOWLEDGMENTS

This research was supported by the National Science and Technology Major Special Project 2016ZX05024-006-005.

## REFERENCES

- (1) Wen, Y. Research on molecular diffusion behavior and numerical simulation of gas injection development in fractured reservoirs. Ph.D. Thesis, Southwest Petroleum Institute, 2005, pp 34–37.
- (2) Yang, H.; Kang, W.; Yin, X.; Tang, X.; Song, S.; Lashari, Z. A.; Bai, B.; Sarsenbekuly, B. Research on matching mechanism between polymer microspheres with different storage modulus and pore throats in the reservoir. *Powder Technol.* **2017**, *313*, 191–200.
- (3) Sun, H.; Wang, T.; Xiao, J. New type of polymer microspheres stepwise deep profile control technology. *Pet. Geo. Rec. Eff.* **2006**, *13*, 77–79. (in Chinese)
- (4) Lei, G.; Zheng, J. Synthesis of pore-throat-scale polymer microspheres and research on new technology of full profile control and oil displacement. *J. China Univ. Pet.* **2007**, *31*, 87–90.
- (5) Liu, C.; An, Y. Deep profile control technology research and mine practice of polymer microspheres. *Drill. Technol.* **2010**, *33*, 62–64.
- (6) Fan, Z.; Cheng, L. Visualization of polymer microsphere profile control and plugging seepage field and mine field test. *Sci. Technol. Eng.* **2012**, *12*, 7543–7546.
- (7) Washburn, E. W. The dynamics of capillary flow. *Phys. Rev.* **1921**, *17*, 273–283.
- (8) Gao, H.; Li, H. Determination of movable fluid percentage and movable fluid porosity in ultra-low permeability sandstone using nuclear magnetic resonance (NMR) technique. *J. Pet. Sci. Eng.* **2015**, *133*, 258–267.
- (9) Yang, H.; Huang, Z.; Zhang, M. Research on flooding performance of nano-polymer microspheres with different particle size combinations. *J. Yangtze Univ.* **2020**, *17*, 36–41.
- (10) Liu, J.; Dai, L.; Li, X. Research on Z1 polymer microsphere reservoir adaptability and control flooding effect. *Petrochem. Ind.* **2020**, *11*, 1–5.
- (11) Jiao, S.; Guan, H.; Guo, X.; Fang, Z.; Fan, L. Cementing slurry design for HT/HP and high H<sub>2</sub>S content gas wells. *Nat. Gas Explor. Dev.* **2010**, *33*, 60–63.
- (12) Wang, Y.; Weng, G.; Li, J.; Li, L. Long core displacement experiments for fractured carbonate reservoir of Gbeibe oilfield in Syria. *Dril. Pro. Tec.* **2015**, *38*, 95–97.
- (13) Lv, B.; MaCheng, Q. H. Simulation research on CO<sub>2</sub> and water flooding of long core test. *Nat. Gas Oil* **2015**, *33*, 69–72.
- (14) Mandelbrot, B. B.; Passoja, D. E.; Paullay, A. J. Fractal character of fracture surfaces of metals. *Nature* **1984**, *308*, 721–722.
- (15) Zhang, Z.; Weller, A. Fractal dimension of pore space geometry of an Eocene sandstone formation. *Geophysics* **2014**, *79*, D377–D387.
- (16) He, Y.; Wu, N. A new method to determine the fractal dimension of pore structure. *Pet. Geo. Expt.* **1999**, *21*, 372–375.
- (17) Feng, X.; Zhu, H. Micro-pore structure and fractal characteristics of tight sandstone reservoirs in the Lower Shihezi Formation in Sulige area, Ordos Basin. *Geol. Sci. Tec. Inf.* **2019**, *38*, 147–156.
- (18) Hua, Z.; Lin, M.; Guo, J.; Xu, F.; Li, Z.; Li, M. Study on plugging performance of cross-linked polymer microspheres with reservoir pores. *J. Pet. Sci. Eng.* **2013**, *105*, 70–75.
- (19) Lin, M.; Zhang, G.; Hua, Z.; Zhao, Q.; Sun, F. Conformation and plugging properties of crosslinked polymer microspheres for profile control. *Colloids Surf., A* **2015**, *477*, 49–54.
- (20) He, D. M.; Nie, F.; Guan, J.; Hu, H. Q.; Zhang, Q. M. Hot Water Extraction and Fixed Bed Pyrolysis for Bitumen Recovery of an Indonesian Oil Sand. *Appl. Mech. Mater.* **2014**, *672–674*, 624–627.
- (21) Zhou, Y.; Yin, D.; Chen, W.; Liu, B.; Zhang, X. Comprehensive review of emulsion and its field application for enhanced oil recovery. *Energy Sci. Eng.* **2019**, *7*, 1046–1058.
- (22) Zhou, Y.; Yin, D.; Cao, R.; Zhang, C. The mechanism for pore-throat scale emulsion displacing residual oil after water flooding. *J. Pet. Sci. Eng.* **2018**, *163*, 519–525.
- (23) Zhong, H.; Qiu, Z.; Chai, J.; Guo, B.; Sun, D.; Liu, J. A preliminary study of the preparation of shale stabilizer with oil sludge from waste to resource. *J. Pet. Sci. Eng.* **2018**, *161*, 50–60.
- (24) Samori, C.; Pezzolesi, L.; Barreiro, D. L.; Galletti, P.; Pasteris, A.; Tagliavini, E. Synthesis of new polyethoxylated tertiary amines and their use as Switchable Hydrophilicity Solvents. *RSC Adv.* **2014**, *4*, 5999–6008.
- (25) Pollet, P.; Eckert, C. A.; Liotta, C. L. Switchable solvents. *Chem. Sci.* **2011**, *2*, 609–614.
- (26) Wilson, A. D.; Stewart, F. F. Structure–function study of tertiary amines as switchable polarity solvents. *RSC Adv.* **2014**, *4*, 11039–11049.
- (27) Kazemzadeh, Y.; Ismail, I.; Rezvani, H.; Sharifi, M.; Riazi, M. Experimental investigation of stability of water in oil emulsions at reservoir conditions: Effect of ion type, ion concentration, and system pressure. *Fuel* **2019**, *243*, 15–27.
- (28) Li, X.; Hou, J.; Sui, H.; Sun, L.; Xu, L. Switchable-Hydrophilicity Triethylamine: Formation and Synergistic Effects of Asphaltenes in Stabilizing Emulsions Droplets. *Materials* **2018**, *11*, 2431.
- (29) Clark, K. A.; Pasternack, D. S. Water Separation of Bitumen from Alberta Bituminous Sand. *Ind. Eng. Chem.* **1932**, *24*, 1410–1416.
- (30) Alvarez-Majmutoy, A.; Gieleciak, R.; Chen, J. Modeling the molecular composition of vacuum residue from oil sand bitumen. *Fuel* **2019**, *241*, 744–752.
- (31) Sitnov, S. A.; Vakhin, A. V.; Mukhamatdinov, I. I.; Onishchenko, Y. V.; Feoktistov, D. A. Effects of calcite and dolomite on conversion of heavy oil under subcritical condition. *Pet. Sci. Technol.* **2019**, *37*, 687–693.
- (32) Bazzaz, M.; Darabi, M. K.; Little, D. N.; Garg, N. A straightforward procedure to characterize nonlinear viscoelastic response of asphalt concrete at high temperatures. *Transp. Res. Rec.* **2018**, *2672*, 481–492.
- (33) Darabi, M. K.; Huang, C.-W.; Bazzaz, M.; Masad, E. A.; Little, D. N. Characterization and validation of the nonlinear viscoelastic-viscoplastic with hardening-relaxation constitutive relationship for asphalt mixtures. *Constr. Build. Mater.* **2019**, *216*, 648–660.
- (34) Ezeakacha, C. P.; Salehi, S.; Hayatdavoudi, A. Experimental Study of Drilling Fluid's Filtration and Mud Cake Evolution in Sandstone Formations. *J. Energy Resour. Technol.* **2017**, *139*, 022912.
- (35) Yoshida, M.; Santosh, M. Energetics of the Solid Earth: An integrated perspective. *Energy Geosci.* **2020**, *1*, 28–35.
- (36) Aminzadeh, R.; Nikazar, M.; Dabir, B. Determining the occurrence time of different stages of asphaltene aggregation using molecular dynamics simulations. *Pet. Sci. Technol.* **2019**, *37*, 2101–2107.
- (37) Hemmati-Sarapardeh, A.; Dabir, B.; Ahmadi, M.; Mohammadi, A. H.; Husein, M. M. Toward mechanistic understanding of asphaltene aggregation behaviour in toluene: The roles of asphaltene structure, aging time, temperature, and ultrasonic radiation. *J. Mol. Liq.* **2018**, *264*, 410–424.
- (38) Jessop, P. G.; Eckert, C. A.; Liotta, C. L.; Heldebrant, D. J. Switchable solvents and methods of use thereof. U.S. Patent 2,008,005,849 A1, 2008, pp 1–3.
- (39) Durelle, J.; Vanderveen, J. R.; Quan, Y.; Chalifoux, C. B.; Kostin, J. E.; Jessop, P. G. Extending the range of switchable-hydrophilicity solvents. *Phys. Chem. Chem. Phys.* **2015**, *17*, 5308–5313.
- (40) Vanderveen, J. R.; Durelle, J.; Jessop, P. G. Design and evaluation of switchable-hydrophilicity solvents. *Green Chem.* **2014**, *16*, 1187–1197.

- (41) Kirmani, F. U. D.; Raza, A.; Gholami, R.; Haidar, M. Z.; Fareed, C. S. Analyzing the effect of steam quality and injection temperature on the performance of steam flooding. *Energy Geosci.* **2021**, *2*, 83–86.
- (42) Durelle, J.; Vanderveen, J. R.; Jessop, P. G. Modelling the behaviour of switchable-hydrophilicity solvents. *Phys. Chem. Chem. Phys.* **2014**, *16*, 5270–5275.
- (43) Boyd, A. R.; Champagne, P.; McGinn, P. J.; MacDougall, K. M.; Melanson, J. E.; Jessop, P. G. Switchable hydrophilicity solvents for lipid extraction from microalgae for biofuel production. *Bioresour. Technol.* **2012**, *118*, 628–632.
- (44) Yang, Y.; Li, X.; Zhang, Y.; Mei, Y.; Ding, R. Insights into moisture content in coals of different ranks by low field nuclear resonance. *Energy Geosci.* **2020**, *1*, 93–99.
- (45) Kang, W.; Li, M. X.; Wu, Y. Y.; Cheng, J.; Gao, R. C. Separation of ethyl acetate and n-heptane by Extractive Distillation. *Mod. Chem. Ind.* **2017**, *37*, 167–170.
- (46) Gu, J.; You, X.; Tao, C.; Li, J.; Shen, W.; Li, J. Improved design and optimization for separating tetrahydrofuran– water azeotrope through extractive distillation with and without heat integration by varying pressure. *Chem. Eng. Res. Des.* **2018**, *133*, 303–313.
- (47) Li, X.; Yang, Z.; Sui, H.; Jain, A.; He, L. A hybrid process for oil-solid separation by a novel multifunctional switchable solvent. *Fuel* **2018**, *221*, 303–310.
- (48) Hong, D.; Cao, J.; Wu, T.; Dang, S.; Hu, W.; Yao, S. Authigenic clay minerals and calcite dissolution influence reservoir quality in tight sandstones: Insights from the central Junggar Basin, NW China. *Energy Geosci.* **2020**, *1*, 8–19.
- (49) Pal, K.; Nogueira Branco, L. d. P.; Heintz, A.; Choi, P.; Liu, Q.; Seidl, P. R.; Gray, M. R. Performance of solvent mixtures for nonaqueous extraction of Alberta oil sands. *Energy Fuels* **2015**, *29*, 2261–2267.
- (50) Aminzadeh, R.; Nikazar, M.; Dabir, B. The effect of nonylphenol on asphaltene aggregation: A molecular dynamics approach. *Pet. Sci. Technol.* **2019**, *37*, 1883–1890.
- (51) Sumbane-Prinsloo, L.; Bunt, J.; Matjie, R.; Piketh, S.; Neomagus, H.; Waanders, F. The effect of particle size on the pollution reduction potential of a South African coal-derived low-smoke fuel. *Energy Geosci.* **2020**, *1*, 165–173.
- (52) Dunn, N. J. H.; Gutama, B.; Noid, W. G. Simple simulation model for exploring the effects of solvent and structure on asphaltene aggregation. *J. Phys. Chem. B* **2019**, *123*, 6111–6122.